# **Inorganic Chemistry**

pubs.acs.org/IC Article

# Phase-Selective Solution Synthesis of Perovskite-Related Cesium Cadmium Chloride Nanoparticles

Cameron F. Holder, Julian Fanghanel, Yihuang Xiong, Ismaila Dabo, and Raymond E. Schaak\*



Cite This: Inorg. Chem. 2020, 59, 11688-11694



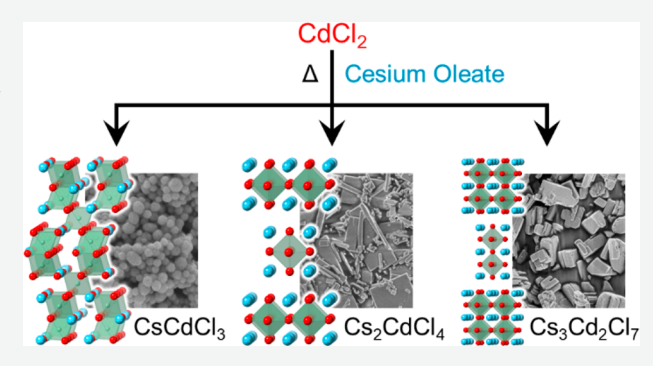
ACCESS

III Metrics & More

Article Recommendations

Supporting Information

ABSTRACT: All-inorganic metal halide perovskite-related phases are semiconducting materials that are of significant interest for a wide range of applications. Nanoparticles of these materials are particularly useful because they permit solution processing while offering unique and tunable properties. Of the many metal halide systems that have been studied extensively, cesium cadmium chlorides remain underexplored, and synthetic routes to access them as nanoscale materials have not been established. Here we demonstrate that a simple solution-phase reaction involving the injection of a cesium oleate solution into a cadmium chloride solution produces three distinct cesium cadmium chlorides: hexagonal CsCdCl<sub>3</sub> and the Ruddlesden–Popper layered perovskites Cs<sub>2</sub>CdCl<sub>4</sub> and Cs<sub>3</sub>Cd<sub>2</sub>Cl<sub>7</sub>. The



phase-selective synthesis emerges from differences in reagent concentrations, temperature, and injection rates. A key variable is the rate at which the cesium oleate solution is injected into the cadmium chloride solution, which is believed to influence the local Cs:Cd concentration during precipitation, leading to control over the phase that forms. Band structure calculations indicate that hexagonal CsCdCl<sub>3</sub> is a direct band gap semiconductor while Cs<sub>2</sub>CdCl<sub>4</sub> and Cs<sub>3</sub>Cd<sub>2</sub>Cl<sub>7</sub> have indirect band gaps. The experimentally determined band gap values for CsCdCl<sub>3</sub>, Cs<sub>2</sub>CdCl<sub>4</sub>, and Cs<sub>3</sub>Cd<sub>2</sub>Cl<sub>7</sub> are 5.13, 4.91, and 4.70 eV, respectively, which places them in a rare category of ultrawide-band-gap semiconductors.

### ■ INTRODUCTION

All-inorganic metal halide perovskites and perovskite-related phases are attracting significant attention for their intriguing properties such as tunable band gaps and long carrier diffusion lengths.<sup>2,3</sup> These properties have led to inorganic metal halide perovskites being investigated as promising materials for numerous applications, including solid-state lighting,<sup>4,5</sup> photocatalysis, 6,7 photovoltaics, 8,9 and thermoelectrics. 10 For example, thin films of tetragonal  $\beta$ -CsPbI<sub>3</sub>, in combination with a hole transport layer, achieved a high power-conversion efficiency in a perovskite solar cell while also exhibiting high stability under continuous illumination in air. Additionally, crystals of Cs2AgInCl6 doped with sodium and bismuth exhibited white light emission with a high photoluminescence quantum yields and a long lifetime. 11 Bulk films and crystals, however, can suffer from low exciton binding energies, and the presence of intrinsic defects can significantly affect the photoluminescence quantum yield. 12 Nanostructured metal halide perovskites can help to circumvent some of these problems.

Over the past few years, the synthesis of nanostructured metal halide perovskites has developed significantly, with diverse synthetic methods producing a broad scope of phases. Solution-based, hot injection methods are particularly powerful, as they permit fine control over nanoparticle size and shape, <sup>13</sup> including cubes, <sup>1,14</sup> nanowires, <sup>15</sup> spheres, <sup>16</sup> and

platelets. 13,14 For example, injecting cesium oleate into a hot solution containing octadecene, oleylamine, oleic acid, and an appropriate  $PbX_2$  salt (X = Cl, Br, I) instantaneously forms the desired metal halide perovskite nanoparticles: i.e., CsPbCl<sub>3</sub>, CsPbBr<sub>3</sub>, and CsPbI<sub>3</sub>. The band gaps of metal halide perovskite nanoparticles can be modified, much like for their bulk counterparts, by changing the identity of the halide or using a mixture of halides. This results in highly tunable photoluminescence with narrow emission line widths that span the entire visible spectrum.<sup>1</sup> The ease of synthesis, the ability to fine-tune the band gap and the nanoparticle size and shape, and the high defect tolerance due to the trap states being located in the conduction or valence band 12,17 make metal halide perovskite nanoparticles of significant interest for a wide range of applications, including light-emitting diodes,<sup>4,5</sup> photodetectors, <sup>18,19</sup> and lasers. <sup>20-</sup>

Solution-based routes to nanocrystals of all-inorganic metal halide perovskites and perovskite-related phases have been

Received: May 28, 2020 Published: August 6, 2020





demonstrated to be important and useful. However, these methods are typically limited to a small number of systems that include the A-site cations Rb<sup>+</sup> and Cs<sup>+</sup> and the B-site cations Pb<sup>2+</sup>, Sn<sup>2+</sup>, and Ge<sup>2+, 23-26</sup> Additional cations have been incorporated, including Ag<sup>+</sup>, Tl<sup>3+</sup>, Bi<sup>3+</sup>, and In<sup>3+,27,28</sup> albeit in the double-perovskite structure. Cadmium-based halide perovskites and perovskite-related phases, which offer unique properties in comparison to their lead halide counterparts, have been studied in the context of doping effects that modify electron paramagnetic resonance and photoluminescent signals, which are important for photon upconversion and higher excited-state luminescence. 29-31 CsCdCl<sub>3</sub> was also considered in the context of a computational screening effort to identify possible metal halide perovskite semiconductors,<sup>3</sup> and CsCdBr<sub>3</sub> was studied for its nonlinear optical properties.<sup>33</sup> However, the synthesis of cadmium-based metal halide perovskites and perovskite-related phases has been limited to bulk-scale single crystals,<sup>34</sup> rather than solution-synthesized nanoscopic phases.

Here we show that cesium cadmium chloride perovskite-related phases can be accessed through solution-based methods related to those that routinely produce other metal halide perovskite nanocrystals, including  $CsPbX_3$  (X = Cl, Br, I). By dissolution of cadmium chloride in a high-boiling-point organic solvent and injection of a solution of cesium oleate at elevated temperatures, three distinct phases can be selectively synthesized as particles having characteristic dimensions in the range of 75-250 nm. The phase selectivity arises from differences in the local concentration of cesium and cadmium ions, the injection rate of cesium oleate, and the reaction temperature. Hexagonal  $CsCdCl_3$  has a three-dimensionally bonded structure that has two face-sharing octahedra that form  $Cd_2Cl_9^{5-}$  subunits, which share corners with six other octahedra (Figure 1a); this structure is often referred to as a

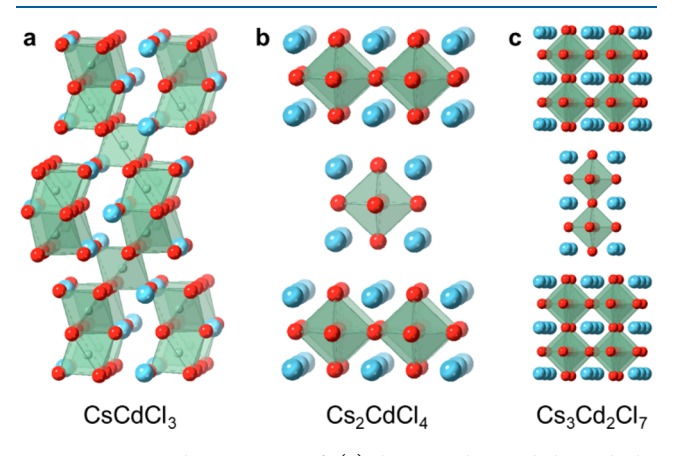


**Figure 1.** Crystal structures of (a) hexagonal  $CsCdCl_3$  and the Ruddlesden–Popper phases (b)  $Cs_2CdCl_4$  and (c)  $Cs_3Cd_2Cl_7$ . The blue, green and red spheres correspond to cesium, cadmium, and chlorine atoms, respectively.

hexagonal perovskite. <sup>35</sup> Cs<sub>2</sub>CdCl<sub>4</sub> (Figure 1b) and Cs<sub>3</sub>Cd<sub>2</sub>Cl<sub>7</sub> (Figure 1c) are Ruddlesden—Popper phases, which are layered intergrowths of perovskite-type cadmium chloride slabs and rock salt type cesium chloride slabs. This synthetic capability bridges the gap between previous syntheses for these phases, which produce bulk-scale crystals using procedures that are not amenable to nanostructuring, and the most commonly used methods for accessing colloidal nanoparticles having tunable

morphologies and sizes. All three of these cesium cadmium chloride phases were found experimentally to have band gaps in the range of 4.70–5.13 eV, which places them in a rare category of ultrawide-band-gap materials that are of interest for applications including deep-ultraviolet optoelectronics and high-power electronics.<sup>36</sup>

### **■ EXPERIMENTAL SECTION**

**Materials.** Cadmium(II) chloride (CdCl<sub>2</sub>, 99.99%) and oleic acid (90%, technical grade) were purchased from Alfa Aesar. Cesium carbonate (Cs<sub>2</sub>CO<sub>3</sub>, 99+%) was purchased from Strem Chemicals. 1-Octadecene (90%, technical grade) and oleylamine (70%, technical grade) were purchased from Sigma-Aldrich. Solvents (hexanes and ethanol) were of analytical grade. All chemicals were used without further purification. Note that cadmium(II) chloride is a toxic reagent that should be handled carefully using appropriate, established safety protocols that are in accordance with the safety data sheet (SDS).

**Preparation of Cesium Oleate.** Cesium oleate was prepared using a modified literature procedure.<sup>37</sup> In a typical synthesis, Cs<sub>2</sub>CO<sub>3</sub> (1.47 g, 4.51 mmol), 1-octadecene (30.9 mL), and oleic acid (14.1 mL) were placed in a three-neck, 100 mL round-bottom flask with a condenser, thermometer adapter, alcohol thermometer, stir bar, and rubber septum. The flask was purged of oxygen by cycling between vacuum and Ar three times. The flask was then heated to 120 °C at 5 °C/min and held at that temperature for 5 h while under a static Ar atmosphere. The solution was cooled to room temperature, and the clear, amber-colored solution was transferred to a septum-capped vial for future use.

Synthesis of CsCdCl<sub>3</sub>. CdCl<sub>2</sub> (84 mg, 0.458 mmol) and 1octadecene (10 mL) were placed in a three-neck, 100 mL roundbottom flask with a condenser, thermometer adapter, alcohol thermometer, magnetic stir bar, and rubber septum. The flask was heated to 100 °C under vacuum for 30 min. After a switch to an Ar atmosphere, a mixture of oleylamine (1 mL) and oleic acid (1 mL) was injected, causing the solution to become clear yellow. The temperature was raised to 300 °C at 5 °C/min, and then 1.4 mL of cesium oleate was injected at a rate of 1.4 mL/min using a syringe pump. Afterward, the reaction flask was placed into a room temperature water bath to cool. The resulting white precipitate was isolated by centrifugation at 13500 rpm for 3 min. The powder was resuspended with a 1/1 mixture of hexanes and ethanol, and the washing procedure was repeated again. The washed powder, which consisted of nanoscopic CsCdCl3, was stored in hexanes for further characterization.

Synthesis of  $Cs_2CdCl_4$ . The procedure was identical with that described above for  $CsCdCl_3$ , except that 53 mg (0.289 mmol) of  $CdCl_2$  was used and the temperature was raised to  $160~^{\circ}C$  at  $5~^{\circ}C/$  min prior to injecting 1.4 mL of cesium oleate at a rate of 1.4 mL/min using a syringe pump.

**Synthesis of Cs<sub>3</sub>Cd<sub>2</sub>Cl<sub>7</sub>.** The procedure was identical with that described above for CsCdCl<sub>3</sub>, except that 62 mg (0.338 mmol) of CdCl<sub>2</sub> was used and the temperature was raised to 240 °C at 5 °C/min prior to injecting 1.4 mL of cesium oleate at a rate of 1.4 mL/min using a syringe pump. For this reaction, it is important for the solution to change from a clear yellow to a milky white before the cesium oleate is injected. This change should occur around 220 °C.

**Characterization.** Powder X-ray diffraction (XRD) data were collected on a Bruker D8 Advance X-ray diffractometer with Cu  $K\alpha$  radiation ( $\lambda=1.5406$  Å). Scanning electron microscopy (SEM) images and energy dispersive spectroscopy (EDS) data, including element maps, were collected on a Verios G4 XHR FESEM instrument. Images were collected at an accelerating voltage of 3 keV and a working distance of 2–3 mm, while maps were collected at 10 keV and a working distance of 4 mm. To mitigate charging effects on the Cs<sub>3</sub>Cd<sub>2</sub>Cl<sub>7</sub> particles, beam deceleration was used to retard the electron beam energy to a landing voltage of 1 keV. For EDS mapping, the L $\alpha_1$  lines for Cs (4.29 keV) and Cd (3.13 keV) were used while the  $K\alpha_1$  line was used for Cl (2.62 keV). Diffuse reflectance UV–vis spectroscopy data were acquired using a

PerkinElmer Lambda 950 UV—vis—NIR spectrophotometer utilizing a 150 mm integrating sphere collecting data from 200 to 800 nm, taking 1 nm steps, and using a 4 nm slit width in the diffuse reflection mode. The reference spectrum for total reflectance (pure white) was measured against a Spectralon disk. A concentrated suspension of nanoparticles was drop-cast onto a glass slide until a uniform, thick, and opaque spot was observed.

DFT Calculations. First-principles calculations were performed to investigate the band gaps and band structures of the hexagonal CsCdCl<sub>3</sub> crystal and the Ruddlesden-Popper Cs<sub>2</sub>CdCl<sub>4</sub> and Cs<sub>3</sub>Cd<sub>2</sub>Cl<sub>7</sub> phases. The self-consistent-field calculations were initially performed at the Perdew-Burke-Ernzerhof (PBE)<sup>38</sup> semilocal level of density functional theory using the projected augmented wave (PAW)<sup>39,40</sup> method implemented in the Vienna Ab initio Simulation Package (VASP).<sup>41</sup> The plane-wave basis energy cutoff was set to 520 eV. Brillouin zones of the perovskites were sampled with Gaussian smearing, with a Γ-centered Monkhorst–Pack grid density of 0.04/Å. The atomic positions and the lattice vectors of the perovskite bulk structures were fully optimized to converge the total energy and force within less than  $10^{-6}$  eV and 0.01 eV/Å, respectively. For the band structure calculations, on consideration of the known underestimation of the band gap at the semilocal level, the hybrid Heyd-Scuseria-Ernzerhof functional (HSE06)<sup>42</sup> was applied. The lattice constants that were computationally determined through structure relaxation as well as the simulated lattice constants are shown in Table S1. The difference between the calculated and simulated lattice constants was small, ranging from 0.0012 to 0.12 Å. Therefore, both the PBE and HSE06 functionals predicted lattice constants that are consistent with experimental observations.

#### RESULTS AND DISCUSSION

CsCdCl<sub>3</sub>, Cs<sub>2</sub>CdCl<sub>4</sub>, and Cs<sub>3</sub>Cd<sub>2</sub>Cl<sub>7</sub> were synthesized using a solution-based method involving the injection of a cesium oleate solution into a heated CdCl<sub>2</sub> solution, as described in the Experimental Section and outlined in the reaction schemes in Figure S1. All three synthesized phases were stable when they were stored under ambient conditions but unstable in highly polar solvents.

Figure 2a shows the experimental powder XRD pattern for the CsCdCl<sub>3</sub> product, which matches well with the simulated pattern for hexagonal CsCdCl<sub>3</sub>.<sup>43</sup> The structure of hexagonal CsCdCl<sub>3</sub>, highlighted in Figure 1a, shows the two face-sharing octahedra that comprise the Cd<sub>2</sub>Cl<sub>9</sub><sup>5-</sup> subunit mentioned above, which share corners with six other distinct octahedra.<sup>44</sup> SEM-EDS element maps and spectra, shown in Figure 2b and Figure S2, confirm that cesium, cadmium, and chlorine were uniformly distributed throughout the sample. There was no microscopic evidence of secondary phases or amorphous components: i.e., no regions have significantly different morphologies or compositions. The SEM image shown in Figure 2c reveals roughly spherical particles with diameters of approximately 100 nm. The isotropic morphology observed by SEM is consistent with the XRD data, which does not show evidence of a preferred orientation. The particle size observed by SEM is also consistent with the XRD data, which do not have significantly broadened peaks, as would be expected for smaller particle sizes.

When the amounts of cesium oleate and CdCl<sub>2</sub> used in the reaction were changed, as well as the reaction temperature, it was possible to also synthesize two Ruddlesden–Popper phases,  $A_{n+1}B_nX_{3n+1}$ , in the Cs–Cd–Cl system. Both the n=1 phase, Cs<sub>2</sub>CdCl<sub>4</sub>, and the n=2 phase, Cs<sub>3</sub>Cd<sub>2</sub>Cl<sub>7</sub>, are intergrowth structures of 2D perovskite layers, where n is the number of perovskite layers, interleaved between a rock salt layer (Figure 1b,c).<sup>45</sup>

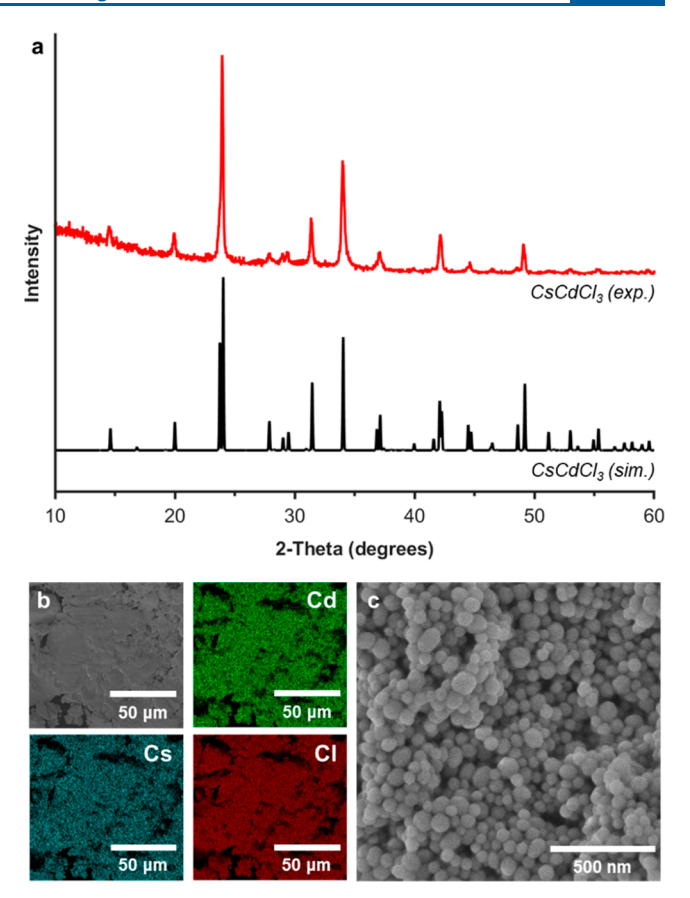


**Figure 2.** (a) Experimental and simulated powder XRD patterns for hexagonal CsCdCl<sub>3</sub>. (b) Low-magnification SEM image and corresponding SEM-EDS element maps for Cd, Cs, and Cl. (c) Higher magnification SEM image showing the spherical morphology of the CsCdCl<sub>3</sub> particles.

The experimental XRD and simulated reference patterns of the n = 1 Ruddlesden-Popper phase,  $Cs_2CdCl_4$ , are shown in Figure 3a. 43 The XRD data indicate that Cs<sub>2</sub>CdCl<sub>4</sub> formed with no crystalline impurities, and the SEM-EDS element maps and spectra (Figure 3b and Figure S2) confirm that the expected elements are uniformly distributed. In contrast to CsCdCl<sub>3</sub>, which produced roughly spherical particles, the Cs<sub>2</sub>CdCl<sub>4</sub> particles appear as a mixture of large rectangular plates and rods that have dimensions up to 5  $\mu$ m, as shown in the SEM image in Figure 3c. The anisotropic morphology observed microscopically, which is expected on the basis of the layered crystal structure, is validated in the bulk sample by the XRD data. In the XRD pattern for Cs<sub>2</sub>CdCl<sub>4</sub> in Figure 3a, the intensities of the peaks corresponding to the {001} planes are significantly enhanced in comparison to the simulated pattern, indicating a preferred orientation perpendicular to the [001] direction. This preferred orientation is consistent with, and expected for, both platelets and rods which grow such that the {00l} planes are parallel to the basal plane. Additionally, the {00l} XRD peaks are broadened relative to the other peaks. Scherrer analysis of the {00l} peaks indicates an average grain thickness of 11 nm, which is consistent with the anisotropic morphology and provides an estimate for the thickness of the Cs<sub>2</sub>CdCl<sub>4</sub> platelets and rods.

XRD data for the n=2 Ruddlesden-Popper phase,  $Cs_3Cd_2Cl_7$ , are shown in Figure 4a. A comparison of the experimental and simulated XRD data<sup>34</sup> confirms the

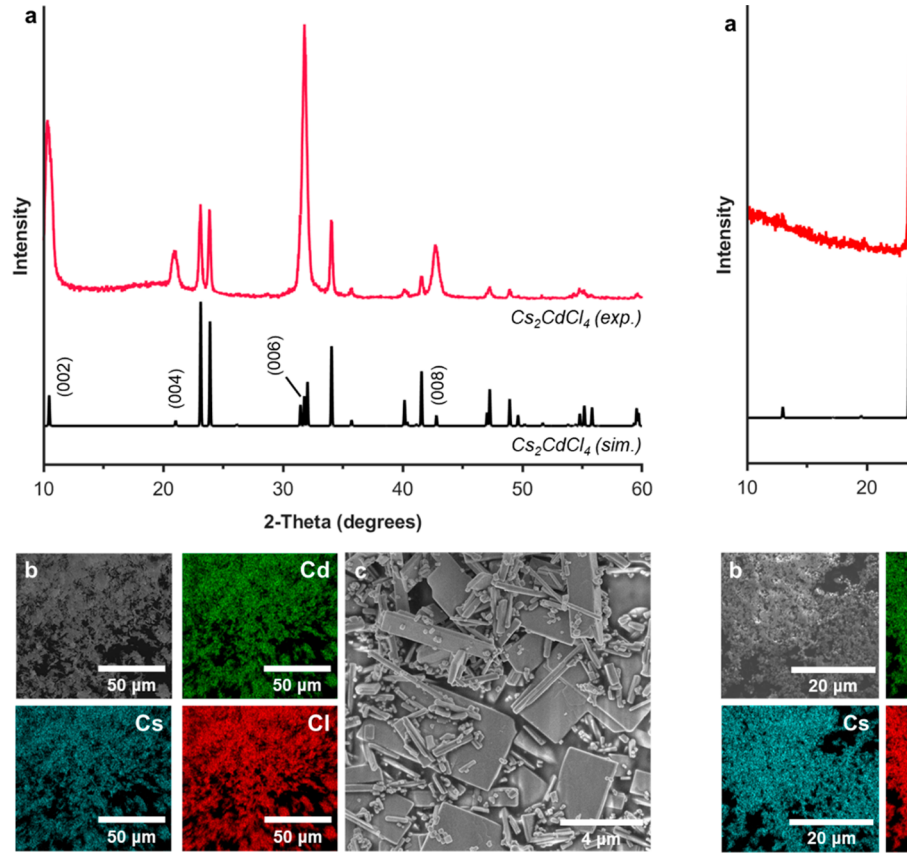


**Figure 3.** (a) Experimental and simulated powder XRD patterns for Cs<sub>2</sub>CdCl<sub>4</sub>. (b) Low-magnification SEM image and corresponding SEM-EDS element maps for Cd, Cs, and Cl. (c) High-magnification SEM image showing the micrometer-sized Cs<sub>2</sub>CdCl<sub>4</sub> plates and rods.

formation of Cs<sub>3</sub>Cd<sub>2</sub>Cl<sub>7</sub> with no observable impurities, while the SEM-EDS element maps and spectra in Figure 4b and Figure S2 indicate that, like the other phases, the three constituent elements are evenly distributed throughout the sample. The SEM image in Figure 4c shows that the particles are anisotropic, similar to those of Cs2CdCl4. However, the morphologies of the Cs<sub>3</sub>Cd<sub>2</sub>Cl<sub>7</sub> particles are noticeably different. The SEM image reveals that most of the particles form rectangular prisms with lateral dimensions ranging from 250 nm to 1 μm. In contrast to Cs<sub>2</sub>CdCl<sub>4</sub>, which exhibited a preferred orientation perpendicular to the [001] direction, the {110} family of planes in Cs<sub>3</sub>Cd<sub>2</sub>Cl<sub>7</sub> have slightly higher relative intensities in comparison to the simulated pattern. While this preferred orientation direction differs from that seen in most layered compounds (i.e., the layer stacking axis), it has been observed in other Ruddlesden-Popper phases as particles and thin films 46,47 and therefore is not unexpected. In these other Ruddlesden-Popper systems, the observation of a preferred orientation perpendicular to the [110], instead of [001], direction was attributed to the rate of particle growth. 46 It is possible that the observed differences in morphology and preferred orientation between the Cs<sub>2</sub>CdCl<sub>4</sub> platelets and the Cs<sub>3</sub>Cd<sub>2</sub>Cl<sub>7</sub> prisms arises from faster crystal growth kinetics of the Cs2CdCl4 phase, which can be altered through the injection rate of cesium oleate, as discussed in further detail below. It is also possible that slight differences in ligand binding affinities to the exposed facets of Cs2CdCl4 vs

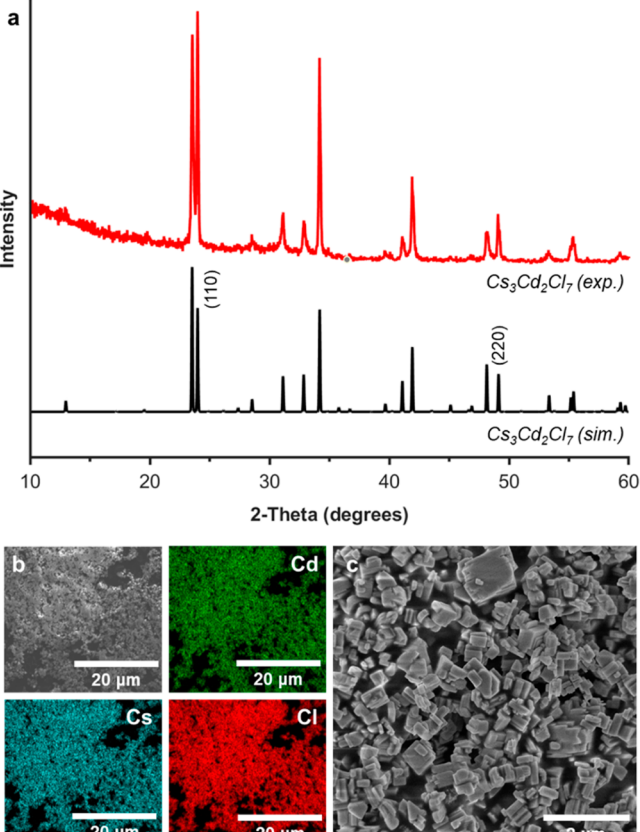


**Figure 4.** (a) Experimental and simulated powder XRD patterns for  $Cs_3Cd_2Cl_7$ . (b) Low-magnification SEM image and corresponding SEM-EDS element maps for Cd, Cs, and Cl. (c) High-magnification SEM image showing the  $Cs_3Cd_2Cl_7$  platelets.

 $Cs_3Cd_2Cl_7$  could play a role in the observed differences in morphology and preferred orientation.

The phase-selective synthesis of hexagonal  $CsCdCl_3$  and Ruddlesden–Popper  $Cs_2CdCl_4$  and  $Cs_3Cd_2Cl_7$ , using the same platform, is significant and important, as different compounds in the same phase diagram typically have different properties. It is therefore useful to identify how subtle differences in reaction parameters lead to phase selectivity. All three reactions involve the same injection volume of cesium oleate, and therefore the cesium reagent concentration remains constant. The key procedural differences, determined on the basis of observations of experiments run under a variety of conditions, involve differences in the concentrations of cesium and cadmium, the injection rate of cesium oleate, and the reaction temperature.

Consider hexagonal CsCdCl<sub>3</sub>, which forms as a pure phase when cesium oleate is slowly injected into the solution of CdCl<sub>2</sub> at 300 °C, such that the cesium and cadmium ion concentrations are equivalent. When this reaction is run at a lower temperature, cubic CsCdCl<sub>3</sub> begins to form, although not as a pure phase; it is always present, in an ~1:1 ratio, with hexagonal CsCdCl<sub>3</sub> (Figure S3). Hexagonal CsCdCl<sub>3</sub> is the thermodynamically preferred structure, and so its formation at a higher temperature is expected, although the observation of some cubic perovskite-type CsCdCl<sub>3</sub> suggests that this metastable polymorph may be accessible as a pure phase with further optimization. When the injection rate of the cesium oleate into the cadmium chloride is increased significantly, from 1.4 mL/min to 1.4 mL/s, while the same

cesium and cadmium ion concentrations and 300 °C temperature are maintained, Cs<sub>2</sub>CdCl<sub>4</sub> begins to form, along with hexagonal CsCdCl<sub>3</sub>. Likewise, when the reaction that forms phase-pure Cs<sub>3</sub>Cd<sub>2</sub>Cl<sub>7</sub> is carried out with a faster injection rate (1.4 mL/s instead of 1.4 mL/min), Cs<sub>2</sub>CdCl<sub>4</sub>, the most Cs-rich phase, begins to form (Figure S4). However, when the reaction that forms phase-pure Cs<sub>2</sub>CdCl<sub>4</sub> is carried out at the faster injection rate, Cs2CdCl4 still forms (Figure S5). On the basis of these results, we speculate that a faster injection rate increases the local concentration of Cs relative to Cd to begin favoring more Cs rich phases, resulting in the preferential formation of the most Cs rich phase, Cs<sub>2</sub>CdCl<sub>4</sub>, at faster rates of cesium oleate injection. These observations led to the identification of the optimized conditions that were used to generate phase-pure products and also provided some insights into how the various phases form.

CsCdCl<sub>3</sub>, which had been previously synthesized as single crystals, was found in several studies to have a band gap that is on the order of 5 eV, <sup>48,49</sup> which places it in a rare category of ultrawide-band-gap materials. Anticipating that the different Cs-Cd-Cl phases would have different band gaps, we used diffuse reflectance UV-vis spectroscopy to determine the optical band gaps of our nanoscopic CsCdCl<sub>3</sub>, Cs<sub>2</sub>CdCl<sub>4</sub>, and Cs<sub>3</sub>Cd<sub>2</sub>Cl<sub>7</sub> materials. The diffuse reflectance spectra for all three phases are shown in Figure 5a and Figure S6. The onset

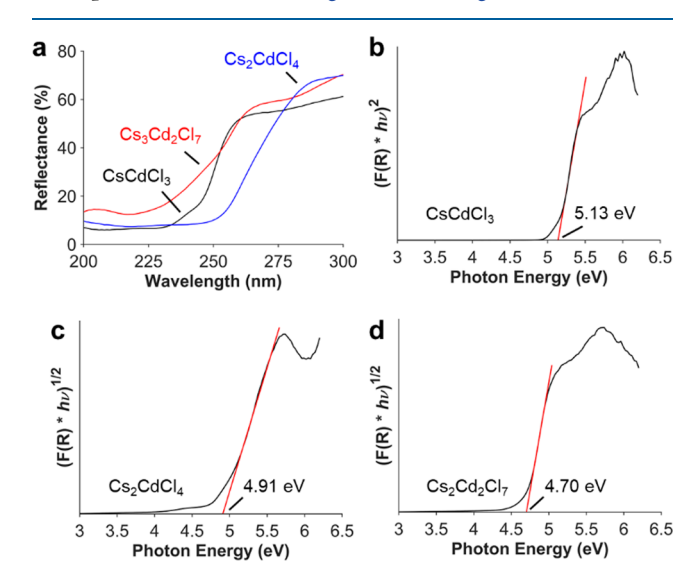


**Figure 5.** (a) Diffuse reflectance spectra for CsCdCl<sub>3</sub>, Cs<sub>2</sub>CdCl<sub>4</sub>, and Cs<sub>3</sub>Cd<sub>2</sub>Cl<sub>7</sub> particles. (b–d) Tauc plots of CsCdCl<sub>3</sub>, Cs<sub>2</sub>CdCl<sub>4</sub>, and Cs<sub>3</sub>Cd<sub>2</sub>Cl<sub>7</sub>, respectively, with the experimental band-gap values.

of absorption for all three phases occurs in the range of 225–275 nm;  $Cs_2CdCl_4$  has the highest absorption onset at 280 nm, and  $Cs_3Cd_2Cl_7$  has the lowest absorption onset at 255 nm.

First-principles calculations were performed to determine if each phase had a direct or an indirect electronic transition. By calculation of the band structures along the high-symmetry directions for all of the crystal structures at the PBE level, hexagonal CsCdCl<sub>3</sub> was found to have a direct band gap, while Cs<sub>2</sub>CdCl<sub>4</sub> and Cs<sub>3</sub>Cd<sub>2</sub>Cl<sub>7</sub> had indirect band gaps (Figures S7–S9). Using the square root or square of the Kubelka–Munk function for indirect vs direct transitions, respectively, the diffuse reflectance spectra were transformed into the Tauc plots shown in Figure 5b–d. An analysis of the Tauc plots indicated that the band gaps of CsCdCl<sub>3</sub>, Cs<sub>2</sub>CdCl<sub>4</sub>, and

Cs<sub>3</sub>Cd<sub>2</sub>Cl<sub>7</sub> were 5.13, 4.91, and 4.70 eV, respectively. The observed band-gap values for the cesium cadmium chloride particles are considerably larger than for cesium lead chloride nanoparticles, which have band gaps of around 3 eV. The larger band gaps of the cadmium vs lead compounds are attributed to the larger Cd-Cl vs Pb-Cl electronegativity differences. The experimental band gap for CsCdCl<sub>3</sub>, determined here to be 5.13 eV, falls within the previously reported range of band gaps for this material. 48,49 It is wellknown that semilocal (PBE) calculations significantly underestimate band gaps. Therefore, we employed the hybrid HSE06 functional to achieve higher predictive accuracy. Using this approach, CsCdCl<sub>3</sub>, Cs<sub>2</sub>CdCl<sub>4</sub>, and Cs<sub>3</sub>Cd<sub>2</sub>Cl<sub>7</sub> were calculated to have band gaps of 3.50, 4.20, and 3.43 eV, respectively, and the HSE06 predictions are thus in reasonable accordance with experiments. The experimental and computational band gaps of CsCdCl<sub>3</sub>, Cs<sub>2</sub>CdCl<sub>4</sub>, and Cs<sub>3</sub>Cd<sub>2</sub>Cl<sub>7</sub> are larger than 3.4 eV, which places them in the category of ultrawide-band-gap materials.<sup>36</sup> The total and projected densities of states for all three synthesized phases were also calculated (Figure S10). It was observed that the valence band edge for the three structures was primarily composed of the Cl p orbitals with some added contribution from the Cd d orbitals. Similarly, for the conduction band edges, the Cd s orbital was the primary contributor, with additional contributions from the Cl p orbitals.

#### CONCLUSIONS

Three distinct cesium cadmium chloride compounds were synthesized as nanoscopic particles using a low-temperature solution-based method. The hexagonal perovskite-related CsCdCl<sub>3</sub> phase formed as spherical particles and had a direct band gap of 5.13 eV. The Ruddlesden-Popper phases Cs<sub>2</sub>CdCl<sub>4</sub> and Cs<sub>3</sub>Cd<sub>2</sub>Cl<sub>7</sub> formed as anisotropic plates/rods and rectangular prisms and had indirect band gaps of 4.91 and 4.70 eV, respectively. Phase selectivity was achieved through differences in the precursor concentrations of cesium and cadmium ions, the injection rate of cesium oleate, and the reaction temperature. The injection rate, in particular, was found to significantly influence the phase that formed; a faster rate of injecting cesium oleate correlated with the formation of more Cs rich phases, presumably due to higher local concentrations of Cs relative to Cd. It is anticipated that this phase-selective synthesis could be further developed and modified to produce the types of size- and shape-controlled nanoparticles that are advantageous for applications as lightemitting diodes, photodetectors, and lasers. As ultrawide-bandgap materials, they are especially interesting as potential components for deep ultraviolet optoelectronics, although the toxicity of cadmium may limit their practical utility and/or require methods to ensure stability under operating conditions.

#### ASSOCIATED CONTENT

### Supporting Information

. The Supporting Information is available free of charge at https://pubs.acs.org/doi/10.1021/acs.inorgchem.0c01574.

Supplemental XRD patterns and EDS spectra, table of calculated and experimental lattice parameters, and calculated band structures of  $CsCdCl_3$ ,  $Cs_2CdCl_4$ , and  $Cs_3Cd_2Cl_7$  (PDF)

## AUTHOR INFORMATION

#### **Corresponding Author**

Raymond E. Schaak — Department of Chemistry, Department of Chemical Engineering, and Materials Research Institute, The Pennsylvania State University, University Park, Pennsylvania 16802, United States; orcid.org/0000-0002-7468-8181; Email: res20@psu.edu

#### **Authors**

Cameron F. Holder — Department of Chemistry, The Pennsylvania State University, University Park, Pennsylvania 16802, United States; oorcid.org/0000-0003-1036-4142

Julian Fanghanel – Department of Chemistry and Department of Materials Science and Engineering, The Pennsylvania State University, University Park, Pennsylvania 16802, United States

Yihuang Xiong — Department of Materials Science and Engineering, The Pennsylvania State University, University Park, Pennsylvania 16802, United States; orcid.org/0000-0001-7809-6047

Ismaila Dabo — Department of Materials Science and Engineering, The Pennsylvania State University, University Park, Pennsylvania 16802, United States; ◎ orcid.org/0000-0003-0742-030X

Complete contact information is available at: https://pubs.acs.org/10.1021/acs.inorgchem.0c01574

#### Notes

The authors declare no competing financial interest.

# ACKNOWLEDGMENTS

The synthetic work (C.F.H., R.E.S.) was supported by the American Chemical Society Petroleum Research Fund under grant #58373-ND5. The computational work (J.F., Y.X., I.D.) was supported by the National Science Foundation under grant DMREF-1729338. SEM-EDS images and diffuse reflectance UV—vis spectra were collected at the Materials Characterization Lab of the Penn State Materials Research Institute.

# REFERENCES

- (1) Protesescu, L.; Yakunin, S.; Bodnarchuk, M. I.; Krieg, F.; Caputo, R.; Hendon, C. H.; Yang, R. X.; Walsh, A.; Kovalenko, M. V. Nanocrystals of Cesium Lead Halide Perovskites (CsPbX<sub>3</sub>, X = Cl, Br, and I): Novel Optoelectronic Materials Showing Bright Emission with Wide Color Gamut. *Nano Lett.* **2015**, *15*, 3692–3696.
- (2) Li, B.; Zhang, Y.; Fu, L.; Yu, T.; Zhou, S.; Zhang, L.; Yin, L. Surface Passivation Engineering Strategy to Fully-Inorganic Cubic CsPbI<sub>3</sub> Perovskites for High-Performance Solar Cells. *Nat. Commun.* **2018**, *9*, 1–8.
- (3) Li, B.; Zhang, Y.; Zhang, L.; Yin, L. PbCl<sub>2</sub>-Tuned Inorganic Cubic CsPbBr<sub>3</sub>(Cl) Perovskite Solar Cells with Enhanced Electron Lifetime, Diffusion Length and Photovoltaic Performance. *J. Power Sources* **2017**, *360*, 11–20.
- (4) Jiang, M.; Hu, Z.; Liu, Z.; Wu, Z.; Ono, L. K.; Qi, Y. Engineering Green-to-Blue Emitting CsPbBr<sub>3</sub> Quantum-Dot Films with Efficient Ligand Passivation. *ACS Energy Lett.* **2019**, *4*, 2731–2738.
- (5) Lin, K.; Xing, J.; Quan, L. N.; de Arquer, F. P. G.; Gong, X.; Lu, J.; Xie, L.; Zhao, W.; Zhang, D.; Yan, C.; Li, W.; Liu, X.; Lu, Y.; Kirman, J.; Sargent, E. H.; Xiong, Q.; Wei, Z. Perovskite Light-Emitting Diodes with External Quantum Efficiency Exceeding 20 per Cent. *Nature* 2018, 562, 245–248.
- (6) Bhosale, S. S.; Kharade, A. K.; Jokar, E.; Fathi, A.; Chang, S. M.; Diau, E. W. G. Mechanism of Photocatalytic CO<sub>2</sub> Reduction by Bismuth-Based Perovskite Nanocrystals at the Gas-Solid Interface. *J. Am. Chem. Soc.* **2019**, *141*, 20434–20442.

- (7) Wang, T.; Yue, D.; Li, X.; Zhao, Y. Lead-Free Double Perovskite Cs<sub>2</sub>AgBiBr<sub>6</sub>/RGO Composite for Efficient Visible Light Photocatalytic H<sub>2</sub> Evolution. *Appl. Catal.*, B **2020**, 268, 118399.
- (8) Liu, C.; Li, W.; Zhang, C.; Ma, Y.; Fan, J.; Mai, Y. All-Inorganic CsPbI<sub>2</sub>Br Perovskite Solar Cells with High Efficiency Exceeding 13%. *J. Am. Chem. Soc.* **2018**, *140*, 3825–3828.
- (9) Wang, Y.; Ibrahim Dar, M.; Ono, L. K.; Zhang, T.; Kan, M.; Li, Y.; Zhang, L.; Wang, X.; Yang, Y.; Gao, X.; Qi, Y.; Grätzel, M.; Zhao, Y. Thermodynamically Stabilized B-CsPbI<sub>3</sub>-Based Perovskite Solar Cells with Efficiencies > 18%. *Science* **2019**, *365*, 591–595.
- (10) Xie, H.; Hao, S.; Bao, J.; Slade, T. J.; Snyder, G. J.; Wolverton, C.; Kanatzidis, M. G. All-Inorganic Halide Perovskites as Potential Thermoelectric Materials: Dynamic Cation off-Centering Induces Ultralow Thermal Conductivity. *J. Am. Chem. Soc.* **2020**, *142*, 9553.
- (11) Luo, J.; Wang, X.; Li, S.; Liu, J.; Guo, Y.; Niu, G.; Yao, L.; Fu, Y.; Gao, L.; Dong, Q.; Zhao, C.; Leng, M.; Ma, F.; Liang, W.; Wang, L.; Jin, S.; Han, J.; Zhang, L.; Etheridge, J.; Wang, J.; Yan, Y.; Sargent, E. H.; Tang, J. Efficient and Stable Emission of Warm-White Light from Lead-Free Halide Double Perovskites. *Nature* **2018**, *563*, 541–545.
- (12) Shamsi, J.; Urban, A. S.; Imran, M.; De Trizio, L.; Manna, L. Metal Halide Perovskite Nanocrystals: Synthesis, Post-Synthesis Modifications, and Their Optical Properties. *Chem. Rev.* **2019**, *119*, 3296–3348.
- (13) Pan, A.; He, B.; Fan, X.; Liu, Z.; Urban, J. J.; Alivisatos, A. P.; He, L.; Liu, Y. Insight into the Ligand-Mediated Synthesis of Colloidal CsPbBr<sub>3</sub> Perovskite Nanocrystals: The Role of Organic Acid, Base, and Cesium Precursors. *ACS Nano* **2016**, *10*, 7943–7954.
- (14) Bekenstein, Y.; Koscher, B. A.; Eaton, S. W.; Yang, P.; Alivisatos, A. P. Highly Luminescent Colloidal Nanoplates of Perovskite Cesium Lead Halide and Their Oriented Assemblies. *J. Am. Chem. Soc.* **2015**, *137*, 16008–16011.
- (15) Zhang, D.; Eaton, S. W.; Yu, Y.; Dou, L.; Yang, P. Solution-Phase Synthesis of Cesium Lead Halide Perovskite Nanowires. *J. Am. Chem. Soc.* **2015**, *137*, 9230–9233.
- (16) Liang, Z.; Zhao, S.; Xu, Z.; Qiao, B.; Song, P.; Gao, D.; Xu, X. Shape-Controlled Synthesis of All-Inorganic CsPbBr<sub>3</sub> Perovskite Nanocrystals with Bright Blue Emission. *ACS Appl. Mater. Interfaces* **2016**, *8*, 28824–28830.
- (17) Zhang, Q.; Yin, Y. All-Inorganic Metal Halide Perovskite Nanocrystals: Opportunities and Challenges. ACS Cent. Sci. 2018, 4, 668–679.
- (18) Li, X.; Yu, D.; Chen, J.; Wang, Y.; Cao, F.; Wei, Y.; Wu, Y.; Wang, L.; Zhu, Y.; Sun, Z.; Ji, J.; Shen, Y.; Sun, H.; Zeng, H. Constructing Fast Carrier Tracks into Flexible Perovskite Photodetectors to Greatly Improve Responsivity. ACS Nano 2017, 11, 2015–2023.
- (19) Pan, W.; Wu, H.; Luo, J.; Deng, Z.; Ge, C.; Chen, C.; Jiang, X.; Yin, W. J.; Niu, G.; Zhu, L.; Yin, L.; Zhou, Y.; Xie, Q.; Ke, X.; Sui, M.; Tang, J. Cs<sub>2</sub>AgBiBr<sub>6</sub> Single-Crystal X-Ray Detectors with a Low Detection Limit. *Nat. Photonics* **2017**, *11*, 726–732.
- (20) Eaton, S. W.; Lai, M.; Gibson, N. A.; Wong, A. B.; Dou, L.; Ma, J.; Wang, L. W.; Leone, S. R.; Yang, P. Lasing in Robust Cesium Lead Halide Perovskite Nanowires. *Proc. Natl. Acad. Sci. U. S. A.* **2016**, *113*, 1993–1998
- (21) Pan, J.; Sarmah, S. P.; Murali, B.; Dursun, I.; Peng, W.; Parida, M. R.; Liu, J.; Sinatra, L.; Alyami, N.; Zhao, C.; Alarousu, E.; Ng, T. K.; Ooi, B. S.; Bakr, O. M.; Mohammed, O. F. Air-Stable Surface-Passivated Perovskite Quantum Dots for Ultra-Robust, Single- and Two-Photon-Induced Amplified Spontaneous Emission. *J. Phys. Chem. Lett.* **2015**, *6*, 5027–5033.
- (22) Yakunin, S.; Protesescu, L.; Krieg, F.; Bodnarchuk, M. I.; Nedelcu, G.; Humer, M.; De Luca, G.; Fiebig, M.; Heiss, W.; Kovalenko, M. V. Low-Threshold Amplified Spontaneous Emission and Lasing from Colloidal Nanocrystals of Caesium Lead Halide Perovskites. *Nat. Commun.* **2015**, *6*, 1–9.
- (23) Binyamin, T.; Pedesseau, L.; Remennik, S.; Sawahreh, A.; Even, J.; Etgar, L. Fully Inorganic Mixed Cation Lead Halide Perovskite

- Nanoparticles: A Study at the Atomic Level. *Chem. Mater.* **2020**, 32, 1467–1474.
- (24) Tang, B.; Hu, Y.; Dong, H.; Sun, L.; Zhao, B.; Jiang, X.; Zhang, L. An All-Inorganic Perovskite-Phase Rubidium Lead Bromide Nanolaser. *Angew. Chem., Int. Ed.* **2019**, *58*, 16134–16140.
- (25) Krishnamoorthy, T.; Ding, H.; Yan, C.; Leong, W. L.; Baikie, T.; Zhang, Z.; Sherburne, M.; Li, S.; Asta, M.; Mathews, N.; Mhaisalkar, S. G. Lead-Free Germanium Iodide Perovskite Materials for Photovoltaic Applications. *J. Mater. Chem. A* **2015**, *3*, 23829–23832.
- (26) Jellicoe, T. C.; Richter, J. M.; Glass, H. F. J.; Tabachnyk, M.; Brady, R.; Dutton, S. E.; Rao, A.; Friend, R. H.; Credgington, D.; Greenham, N. C.; Böhm, M. L. Synthesis and Optical Properties of Lead-Free Cesium Tin Halide Perovskite Nanocrystals. *J. Am. Chem. Soc.* 2016, 138, 2941–2944.
- (27) Volonakis, G.; Haghighirad, A. A.; Milot, R. L.; Sio, W. H.; Filip, M. R.; Wenger, B.; Johnston, M. B.; Herz, L. M.; Snaith, H. J.; Giustino, F. Cs<sub>2</sub>InAgCl<sub>6</sub>: A New Lead-Free Halide Double Perovskite with Direct Band Gap. *J. Phys. Chem. Lett.* **2017**, *8*, 772–778.
- (28) Slavney, A. H.; Leppert, L.; Braham, A.; Valdes, S.; Bartesaghi, D.; Savenije, T.; Effrey, J.; Neaton, B.; Karunadasa, H. I. Small-Band-Gap Halide Double Perovskites. *Angew. Chem., Int. Ed.* **2018**, *57*, 12765–12770.
- (29) Mei, Y.; Zheng, W. C. Investigations of the Spin-Hamiltonian Parameters and the Tetragonal Distortion Due to Jahn-Teller Effect for Cu<sup>2+</sup> in Trigonal CsCdCl<sub>3</sub> and CsMgCl<sub>3</sub> Crystals. *Phys. B* **2009**, 404, 1446–1449.
- (30) Wenger, O. S.; Bénard, S.; Gudel, H. U. Crystal Field Effects on the Optical Absorption and Luminescence Properties of Ni<sup>2+</sup>-Doped Chlorides and Bromides: Crossover in the Emitting Higher Excited State. *Inorg. Chem.* **2002**, *41*, 5968–5977.
- (31) Wenger, O. S.; Güdel, H. U. Photon Upconversion Properties of Ni<sup>2+</sup> in Magnetic and Nonmagnetic Chloride Host Lattices. *Inorg. Chem.* **2001**, *40*, 157–164.
- (32) Filip, M. R.; Giustino, F. Computational Screening of Homovalent Lead Substitution in Organic-Inorganic Halide Perovskites. *J. Phys. Chem. C* **2016**, *120*, 166–173.
- (33) Ren, P.; Qin, J.; Chen, C. A Novel Nonlinear Optical Crystal for the IR Region: Noncentrosymmetrically Crystalline CsCdBr<sub>3</sub> and Its Properties. *Inorg. Chem.* **2003**, *42*, 8–10.
- (34) Seifert, H. J.; Koknat, F. W. Neue Alkalichlorocadmate(II) in Den Systemen CsCl/CdCl<sub>2</sub> Und RbCl/CdCl<sub>2</sub>. Z. Anorg. Allg. Chem. **1968**, 357, 314–324.
- (35) Darriet, J.; Subramanian, M. A. Structural Relationships between Compounds Based on the Stacking of Mixed Layers Related to Hexagonal Perovskite-Type Structures. *J. Mater. Chem.* **1995**, *5*, 543–552.
- (36) Tsao, J. Y.; Chowdhury, S.; Hollis, M. A.; Jena, D.; Johnson, N. M.; Jones, K. A.; Kaplar, R. J.; Rajan, S.; Van de Walle, C. G.; Bellotti, E.; Chua, C. L.; Collazo, R.; Coltrin, M. E.; Cooper, J. A.; Evans, K. R.; Graham, S.; Grotjohn, T. A.; Heller, E. R.; Higashiwaki, M.; Islam, M. S.; Juodawlkis, P. W.; Khan, M. A.; Koehler, A. D.; Leach, J. H.; Mishra, U. K.; Nemanich, R. J.; Pilawa-Podgurski, R. C. N.; Shealy, J. B.; Sitar, Z.; Tadjer, M. J.; Witulski, A. F.; Wraback, M.; Simmons, J. A. Ultrawide-Bandgap Semiconductors: Research Opportunities and Challenges. *Adv. Electron. Mater.* **2018**, *4*, 1600501.
- (37) Lu, C.; Wright, M. W.; Ma, X.; Li, H.; Itanze, D. S.; Carter, J. A.; Hewitt, C. A.; Donati, G. L.; Carroll, D. L.; Lundin, P. M.; Geyer, S. M. Cesium Oleate Precursor Preparation for Lead Halide Perovskite Nanocrystal Synthesis: The Influence of Excess Oleic Acid on Achieving Solubility, Conversion, and Reproducibility. *Chem. Mater.* **2019**, *31*, 62–67.
- (38) Perdew, J. P.; Burke, K.; Ernzerhof, M. Generalized Gradient Approximation Made Simple. *Phys. Rev. Lett.* **1996**, *77*, 3865–3868.
- (39) Blöchl, P. E. Projector Augmented-Wave Method. *Phys. Rev. B: Condens. Matter Mater. Phys.* **1994**, *50*, 17953–17979.
- (40) Kresse, G.; Joubert, D. From Ultrasoft Pseudopotentials to the Projector Augmented-Wave Method. *Phys. Rev. B: Condens. Matter Mater. Phys.* **1999**, *59*, 1758–1775.

- (41) Kresse, G.; Furthmüller, J. Efficient Iterative Schemes for Ab Initio Total-Energy Calculations Using a Plane-Wave Basis Set. *Phys. Rev. B: Condens. Matter Mater. Phys.* **1996**, *54*, 11169–11186.
- (42) Krukau, A. V.; Vydrov, O. A.; Izmaylov, A. F.; Scuseria, G. E. Influence of the Exchange Screening Parameter on the Performance of Screened Hybrid Functionals. *J. Chem. Phys.* **2006**, *125*, 224106.
- (43) Siegel, S.; Gebert, E. The Structures of Hexagonal CsCdCl<sub>3</sub> and Tetragonal Cs<sub>2</sub>CdCl<sub>4</sub>. *Acta Crystallogr.* **1964**, *17*, 790.
- (44) Chang, J. R.; McPherson, G. L.; Atwood, J. L. Electron Paramagnetic Resonance Spectra of Vanadium(II) and Nickel(II) Doped into Crystals of Cesium Cadmium Chloride and a Redetermination of the Structure of Cesium Cadmium Chloride. *Inorg. Chem.* 1975, 14, 3079–3085.
- (45) Schaak, R. E.; Mallouk, T. E. Perovskites by Design: A Toolbox of Solid-State Reactions. *Chem. Mater.* **2002**, *14*, 1455–1471.
- (46) Lacotte, M.; David, A.; Rohrer, G. S.; Salvador, P. A.; Prellier, W. Preferential Orientation Relationships in Ca<sub>2</sub>MnO<sub>4</sub> Ruddlesden-Popper Thin Films. *J. Appl. Phys.* **2015**, *118*, 045306.
- (47) Smith, I. C.; Hoke, E. T.; Solis-Ibarra, D.; McGehee, M. D.; Karunadasa, H. I. A Layered Hybrid Perovskite Solar-Cell Absorber with Enhanced Moisture Stability. *Angew. Chem., Int. Ed.* **2014**, *53*, 11232–11235.
- (48) Demirbilek, R.; Çelik Bozdoan, A.; Çalkan, M.; Asan, G.; Özen, G. Electronic Energy Levels of CsCdCl<sub>3</sub>. *J. Lumin.* **2011**, *131*, 1853–1856.
- (49) Dovgii, Y. O.; Kityk, I. V.; Pidzyrailo, S. N.; Khapko, Z. A. Electronic Structure of CsCdCl<sub>3</sub> Single Crystals. *J. Appl. Spectrosc.* **1990**, 53, 1319–1322.